Acta Cryst. (1987). A43, 656-674

Multiplicity Distribution of Reflections in Laue Diffraction

BY D. W. J. CRUICKSHANK,* J. R. HELLIWELL AND K. MOFFAT†

Department of Physics, University of York, Heslington, York YO1 5DD, England and SERC, Daresbury Laboratory, Daresbury, Warrington, Cheshire WA4 4AD, England

(*Received* 6 *January* 1987; *accepted* 2 *April* 1987)

Abstract

If a crystal is illuminated by a polychromatic beam of X-rays, then many orders of each Bragg reflection may be stimulated simultaneously, and overlap exactly in scattering angle. The overlap of these multiple orders along a ray (a central line in reciprocal space) poses a problem for Laue methods. A theory of the distribution of multiple orders as a function of the relevant experimental parameters is presented, with the following conclusions: (1) If the angular acceptance of the detector is unrestricted, then a remarkably large proportion (72·8%) of all Bragg reflections occur on single rays for the case of an infinite range of incident wavelengths. (2) This proportion increases to greater than 83% when more realistic experimental values of λ_{max} and λ_{min} are used. (3) This proportion depends only on the ratio of λ_{max} to λ_{min} and not on the space group, unit-cell dimensions, crystal orientation or the limiting resolution of the crystal d^*_{max} (provided $d^*_{max} < 2/\lambda_{max}$). (4) The total number of single rays, like the total number of all stimulated Bragg reflections, is approximately proportional to the wavelength range. (5) The proportion of reflections at a given resolution d^* that lie on single or double rays depends markedly on d^*, and on the ratio of λ_{max} to λ_{min}; it is generally lower at low resolution than at high. (6) Restricted angular acceptance of the detector can reduce significantly both the proportion and the total number of single rays. (7) Agreement between the theoretical distributions and those derived from analysis of X-ray Laue photographs of macromolecular crystals, and from extensive computer simulations, is good. It is evident that, under a wide variety of experimental conditions, the effect of multiple orders is not a serious limitation on the use of the Laue method for structure determination. The analysis presented has some relevance to polychromatic neutron diffraction.

1. Introduction

The recent availability of synchrotron X-ray sources has renewed interest in Laue diffraction methods, which exploit directly the polychromatic nature of such sources. In preliminary studies, Laue diffraction from protein crystals (Moffat, Szebenyi & Bilderback, 1984; Moffat, Schildkamp, Bilderback & Volz, 1986; Bilderback, Moffat & Szebenyi, 1984; Helliwell, 1984, p. 1468, 1985; Hedman, Hodgson, Helliwell, Liddington & Papiz, 1985) and from small inorganic crystals (Wood, Thompson & Matthewman, 1983; Hails, Harding, Helliwell, Liddington & Papiz, 1984; Harding *et al.*, in preparation) has been examined. These studies suggest that the Laue method possesses advantages over more conventional monochromatic data collection methods. It makes optimum use of the synchrotron radiation spectrum, and affords a reduction in exposure time of several orders of magnitude. The Laue method thus permits very brief exposures in the millisecond time range on strongly scattering protein samples (Bilderback *et al.*, 1984; Hajdu, Machin, Campbell, Clifton, Zurek, Gover & Johnson, 1986; Moffat *et al.*, 1986) and the examination of microcrystals (Hedman *et al.*, 1985). A stationary crystal yields integrated intensities directly, which are relatively insensitive to transient changes in unit-cell dimensions or crystal orientation. A typical Laue diffraction pattern contains many more reflections than a typical monochromatic oscillation pattern. These advantages are particularly appropriate for dynamic experiments, in which the diffraction intensities change rapidly with time in response to a structural perturbation (Wood *et al.*, 1983; Moffat *et al.*, 1984, 1986; Helliwell, 1985).

A fundamental complexity of the Laue method is the multiple-orders problem, which is revealed when Bragg's law is applied to the diffraction of polychromatic X-rays. If a crystal contains a spacing d, it also contains spacings $d/2$, $d/3$, ... or, in general, d/j, where j is any positive integer. Then Bragg's law is simultaneously satisfied by the set of values (d, λ), $(d/2, \lambda/2)$, $(d/3, \lambda/3)$ ... $(d/j, \lambda/j)$.... That is, all orders of a Bragg reflection are exactly superimposed (apart from very small dispersive effects).

The reciprocal-lattice points corresponding to the first and all higher orders lie on a central line passing

* Also Department of Chemistry, UMIST, Manchester, M60 1QD, England.

† Also Section of Biochemistry, Molecular and Cell Biology, Cornell University, Ithaca, New York 14853, USA.

0108-7673/87/050656-19$01.50

through the origin of reciprocal space. We denote such a central line as a ray (§ 2). Each Laue reflection arises from one ray and, conversely, the reciprocal-lattice points along each ray contribute to one, and only one, Laue reflection. A Laue diffraction pattern thus reveals the distribution of rays, whereas a monochromatic diffraction pattern reveals the distribution of reciprocal-lattice points. A Laue reflection may arise from the superposition of Bragg reflections: it may be single, arising from only one spacing, wavelength and structure factor; or double, arising from two; or triple, arising from three, and so on. The multiplcity of a Laue reflection, which we denote by the symbol m, is the number of reciprocal-lattice points along the ray which simultaneously diffract for the given experimental conditions.

The intensity of a multiple Laue reflection is the sum of the intensities of its constituent Bragg reflections, associated with the m reciprocal-lattice points along the ray. Since the individual structure factors are required if the Laue method is to be used for structure determination, the sum must be resolved. The constituents overlap exactly in space, and hence can only be distinguished in energy, in time, or both. In the time-of-flight method with polychromatic neutrons (Schultz, Srinivasan, Teller, Williams & Lukehart, 1984), neutrons of different energies arrive at the detector at different times, and the constituent intensities can be measured separately and directly. There is no time-of-flight method for X-rays, and no suitable energy-sensitive electronic detector exists. X-ray film offers modest energy sensitivity which can be enhanced by interleaving thin metal foils between the films in a multiple film pack. This has permitted the constituent intensities of double Laue reflections to be resolved (Zurek, Papiz, Machin & Helliwell, 1985), but it has not yet been possible to apply this approach satisfactorily to triple or higher multiples.

Clearly, the proportion of single Laue reflections must be very close to 100% for a narrow wavelength range, and must decrease as the range increases. It might be thought that, with a wide wavelength range, few Laue reflections would be single: most would be multiple, arising from several Bragg reflections. Further, the proportion of multiple Laue reflections might be greater for dense reciprocal lattices. If true, structure determination by the Laue method would be greatly hindered [and, indeed, it has been little used for that purpose over the last 50 years (Amorós, Buerger & Amorós, 1975)]. However, two initial studies of protein crystals with dense reciprocal lattices that have employed wide wavelength ranges have been reported. Moffat *et al.* (1984) used a range from 0·73 to 1·77 Å, and Helliwell (1984, p. 1468, 1985) used a range from 0·45 to 2·60 Å. In both studies, a large number of reflections were stimulated simultaneously, of which a remarkably high proportion were single, 92·5 and 77·9% respectively. Furthermore, these and other studies (Hedman *et al.*, 1985; Moffat *et al.*, 1986) established that the lifetime of a typical protein crystal in a 'white beam' of wide wavelength range is enough to allow practical collection of a large quantity of data.

Since a convenient experimental method for resolving constituent X-ray intensities in multiple reflections is lacking, the nature of the distribution of multiple reflections becomes critical. This distribution arises in both neutron and X-ray diffraction, yet no theoretical analysis which might account for the above results seems to have been attempted. We examine this distribution here as a function of the relevant experimental parameters λ_{max}, λ_{min}, d^*_{max}, position in reciprocal space and angular acceptance of the detector. We begin by considering the probability that a randomly selected reciprocal-lattice point is of first, second, third and higher order, and then derive the multiplicity distributions for three models that increase in experimental realism: infinite wavelength range, finite λ_{max} with zero λ_{min}, and arbitrary λ_{max} and λ_{min} (where the latter two models have the additional restriction that $\lambda_{max} < 2/d^*_{max}$). We then remove this restriction and derive the multiplicity distribution and the total number of accessible reciprocal-lattice points that lie on single and double rays. Finally, we consider how these overall multiplicity distributions arise from reflections of a given order in a particular region of reciprocal space and how they are affected by restricted angular acceptance of the detector.

Note added during publication. On the feasibility of the polychromatic Laue method as a means for data acquisition, see also Rabinovich & Lourie (1987).

2. Rays and inner points

For a stationary crystal and white radiation with $\lambda_{max} \geq \lambda \geq \lambda_{min}$, the reciprocal-lattice points (RLPs) whose reflections can be recorded lie between the Ewald spheres of radii $1/\lambda_{max}$ and $1/\lambda_{min}$. These spheres touch at the origin of the reciprocal lattice (Fig. 1*a*), and the wavelength at which any individual RLP diffracts is determined by the reciprocal radius of the Ewald sphere passing through it. There is also a sample resolution limit d^*_{max} ($= 1/d_{min}$), so that no reflections are recorded from RLPs outside a sphere centred at the origin with radius d^*_{max}. The accessible region of reciprocal space, which is cylindrically symmetrical about the incident X-ray beam, may be further limited by experimental restrictions on the scattering angles.

Definitions

A *ray* is a central line from (0, 0, 0) passing through $\mathbf{h} = (h, k, l)$, $2\mathbf{h}$, $3\mathbf{h}$, ..., $n\mathbf{h}$, ... If the indexing has

been referred to a primitive lattice and if the greatest common divisor of h, k, l is 1, then **h** is the *inner point* of the ray. n**h** is the *nth-order point* or nth harmonic on this ray. A ray of *multiplicity* m is one containing m points inside or on the surface of the accessible region of reciprocal space. The accessible region is bounded by the surface S specified by d^*_{max}, λ_{max}, λ_{min} and by any other experimental restrictions. Fig. 1(*b*) shows a ray with five orders inside the d^*_{max} sphere, but of which only two are within the accessible region. The ray is therefore of multiplicity $m = 2$.

As examples $(2, 1, 0)$, $(5, \bar{4}, 1)$, $(15, \bar{14}, \bar{13})$ and $(36, 46, 27)$ are inner points, but $(5, 0, 0)$, $(3, \bar{3}, 0)$, $(8, 6, 4)$, $(14, \bar{21}, 35)$ and $(18, 27, \bar{36})$ are not, having greatest common divisors of 5, 3, 2, 7 and 9 respectively.

What proportion of RLPs are inner points? Does the proportion vary as the indices get larger? The following theorem is relevant. It concerns a property of numbers and is unrelated to the diffraction geometry.

Theorem 1. The probability that a randomly chosen RLP is an inner point is

$$Q = (1-1/2^3)(1-1/3^3)(1-1/5^3)(1-1/7^3) \times (1-1/11^3)\ldots = 0{\cdot}83191\ldots.$$

Proof. The probability that a random integer h, chosen between $-\infty$ and $+\infty$, is divisible by a positive integer n is $1/n$. Thus the probability that three random integers h, k, l have a common integer divisor n is $p_n = 1/n^3$. The probability that 2 is a common divisor is $p_2 = 1/2^3$. The probability q_2 that 2 is *not* a common divisor is $1-1/2^3$. Note that q_2 includes the cases where n is an integer multiple of 2, $n = 4, 6, 8, \ldots$. Similarly $p_3 = 1/3^3$ and $q_3 = 1-1/3^3$. Again note that q_3 includes the cases where $n = 6, 9, 12, \ldots$. Thus the probability that a RLP $\mathbf{h} = (h, k, l)$ is an inner point is given by the probability that the set h, k, l does not have any prime 2, 3, 5, 7, 11, ... as a common divisor. This probability is that stated in the theorem above.

It will be noted that the proof assumes that h, k, l are random integers lying between $-\infty$ and $+\infty$. However, to take a case sometimes pertinent to small-molecule crystallography, if h, k, l were restricted to maximum values of 10, then the terms from $(1-1/11^3)$ onwards would be omitted and, say, the $(1-1/7^3)$ term would be slightly inaccurate as the probability of 7 not being a common factor. But the product is quickly convergent to its limit, and even when only the lowest primes 2 and 3 are considered, the first two terms yield a product 0·843. In macromolecular crystallography the maximum integers are appreciably greater than 10 and any approximation is even smaller. Thus for all crystallographic purposes it will be a good approximation to use Q as the probability that a random RLP is an inner point. This probability is independent of position in reciprocal space and in particular is independent of distance from the origin (except when all indices are very small).

If a region of interest has volume V_R, and V^* is the volume of the reciprocal unit cell, then for $V_R \gg V^*$ the number of RLPs in V_R is approximately $N = V_R/V^*$, and the number of inner points in V_R is $QN = QV_R/V^*$.

It may be added that $1/Q = 1+1/2^3+1/3^3+1/4^3+\ldots = 1{\cdot}202057\ldots = \zeta(3)$, where $\zeta(3)$ is the Riemann zeta function of order 3. The series may be derived by Euler's method of multiplying together the series expansions of the individual terms $(1-1/2^3)^{-1}, \ldots$ in $1/Q$. By direct extension of theorem 1, the probability for n dimensions that a random RLP is an inner point is $1/\zeta(n)$. In two dimensions the probability is $1/\zeta(2) = 6/\pi^2 =$

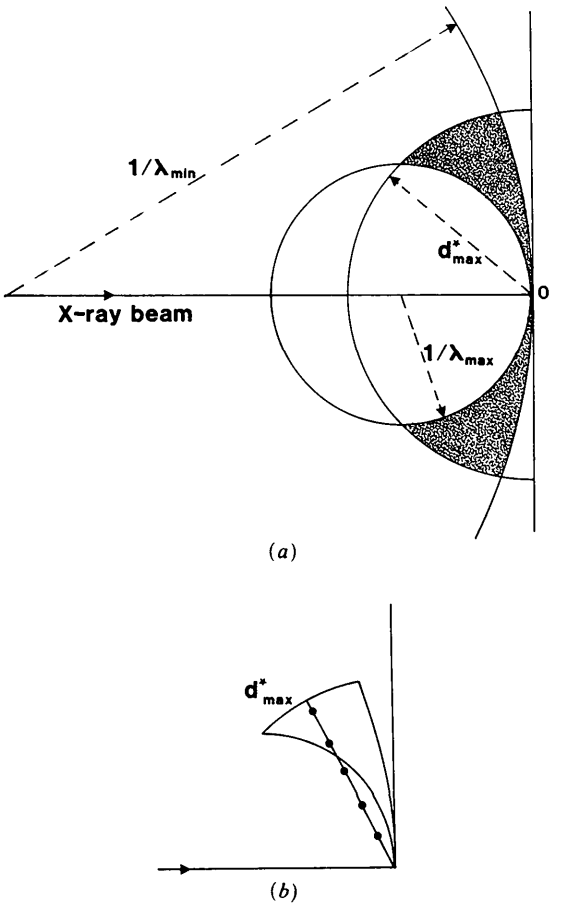

Fig. 1. (*a*) Laue diffraction geometry showing the accessible region of reciprocal space between the Ewald spheres associated with λ_{min} and λ_{max} and the sample resolution limit d^*_{max}. O is the origin of reciprocal space. (*b*) A ray with n orders inside the d^*_{max} sphere can have a recorded multiplicity $m < n$ when $(n-m)$ RLPs are outside the accessible region. The diagram shows the case of $n = 5$ and $m = 2$. Only the upper section of the volume of revolution of the accessible region is shown.

0·6079..., and this is a classical result in the theory of numbers [theorem 332 of Hardy & Wright (1979)]. The problem is sometimes described in terms of the visibility of lattice points from the origin, and for formal mathematical treatments of theorem 1 for n dimensions see Christopher (1956) and Rumsey (1966).

3. Infinite wavelength range: solid-sphere model for arbitrary D^*, infinite λ_{max}, zero λ_{min}

Important features of the distribution of harmonics within a bounding surface can be understood by considering as a model a sphere (Fig. 2) with surface S and radius D^* $(=d^*_{max})$ centred at the origin of reciprocal space containing a large number N of RLPs. This is equivalent to taking $\lambda_{max}=\infty$ and $\lambda_{min}=0$, and replacing the resultant hemisphere by a complete sphere.

Let S_2 be the surface of the sphere of radius $D^*/2$, and T_1 be the shell between D^* and $D^*/2$; let S_3 be the surface of the sphere of radius $D^*/3$, and T_2 be the shell between $D^*/2$ and $D^*/3$; in general let S_n be the surface of the sphere of radius D^*/n, and T_n be the shell between D^*/n and $D^*/(n+1)$.

Theorem 2. All rays of multiplicity n within S have their inner points in the shell T_n.

Proof. An inner point in T_n has reciprocal radius s satisfying $D^*/n \geq s > D^*/(n+1)$. Its nth harmonic has reciprocal radius not greater than $n(D^*/n)=D^*$ and is within S, whereas its $(n+1)$th harmonic has reciprocal radius greater than $(n+1)D^*/(n+1)=D^*$ and is outside S. In particular we note that all $(m=1)$ single rays of S have their inner points in T_1, and all $(m=2)$ double rays have their inner points in T_2.

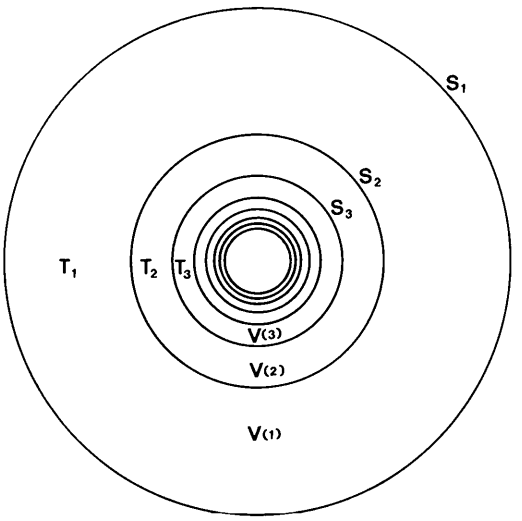

Fig. 2. Infinite-wavelength-range model. A nest of spheres is shown where S_n is the surface of radius D^*/n. T_n is the shell between D^*/n and $D^*/(n+1)$ with volume $V(n)$. The labels identify the cases for $n=1,2,3$.

Table 1. *Multiplicity distribution for infinite wavelength range*

Distribution of RLPs		Distribution of rays	
RLP on single rays	72·8%	Single rays	87·5%
RLP on double rays	14·6	Double rays	8·8
RLP on triple rays	5·4	Triple rays	2·1
RLP on quadruple rays	2·5	Quadruple rays	0·8
RLP on higher-order rays	4·7	Higher-order rays	0·8
	100·0		100·0

3.1. *Distribution of multiplicities*

All single rays start in T_1. The volume of this shell (Fig. 2) is $V(1)=(1-1/2^3)V_R$, where V_R is the volume of the whole region bounded by S. Hence the number of RLPs in T_1 is $(7/8)N$, and since the probability of any RLP being an inner point is Q, the number of single rays emerging through S is $(7/8)QN$.

In general, n-tuple rays start from inner points of probability Q in T_n. This shell is of volume

$$V(n)=[1/n^3-1/(n+1)^3]V_R.$$

so the number of n-tuple rays emerging through S is

$$[1/n^3-1/(n+1)^3]QN.$$

Since every inner point in the whole volume enclosed by S generates a ray, the total number of rays emerging from S is QN. Thus the number of Laue reflections is a fraction Q of the number of accessible RLPs.

The distribution of multiplicities can be expressed either in terms of RLPs or of rays. Thus a proportion $(7/8)Q=72{\cdot}8\%$ of all RLPs lie on single rays and a proportion $7/8=87{\cdot}5\%$ of all rays (Laue reflections) are single rays. Similarly $2(1/2^3-1/3^3)Q=14{\cdot}6\%$ of all RLPs lie on double rays, whereas $(1/2^3-1/3^3)=8{\cdot}8\%$ of all rays are double rays. These results are extended to higher multiplicities in Table 1.

It is notable that even in this extreme case of infinite wavelength range, a substantial majority (72·8%) of RLPs lie on single rays.

3.2. *Other non-re-entrant surfaces*

The above model described the bounding surface S as a sphere. The argument evidently applies as well to an ellipsoid, a cube, a hemisphere defined by arbitrary D^*, $\lambda_{max}=\infty$, $\lambda_{min}=0$, or any surface which is non-re-entrant as seen from the origin. Nesting inner surfaces S_2, S_3,... are defined with linear dimensions shrunk by factors 2,3,... compared with the outer surface S. The volume $V(n)$ of the shell T_n is then the same fraction as before of the total volume V_R and the proportions of rays of the various multiplicities remain unaltered.

4. Model for arbitrary D^* and λ_{max}, zero λ_{min}

For convenience in the following analyses we will refer to the Ewald spheres of radii $1/\lambda_{max}$, $1/\lambda_{min}$, $1/n\lambda_{max}$ *etc.* as the λ_{max}, λ_{min}, $n\lambda_{max}$ *etc.* spheres. The accessible region illustrated earlier in Fig. 1(*a*) is bounded by the spheres for D^*, λ_{max} and λ_{min}. As seen from the origin in Fig. 1(*b*), the bounding surface of this region is re-entrant. Every ray from the origin passes twice through the D^* or λ_{min} spheres. Though the analysis in § 3 therefore cannot be applied directly, it provides a technique for handling the problem.

In this section we consider the case when $\lambda_{min} = 0$, so that the external surface S_e is effectively defined only by the D^* sphere. The internal surface is defined by the λ_{max} sphere, and we assume $\lambda_{max} < 2/D^*$. Fig. 3 shows the upper section of the volume of revolution.

The problem is approached by considering the external and internal surfaces separately. Fig. 4(*a*) divides the region defined by the outer surface S_e into shells separated by segments of spheres of radii $D^*/2$, $D^*/3, \ldots$ as in the solid-sphere model. The multiplicities n of rays having their inner points in each shell are also shown. Fig. 4(*b*) shows the internal surface S_i defined by the λ_{max} sphere. Proportionately shrunk surfaces are defined by spheres of radii $1/2\lambda_{max}$, $1/3\lambda_{max}, \ldots$. A ray having an inner point between the $2\lambda_{max}$ and $3\lambda_{max}$ spheres will also have a second-order point before the ray enters the accessible region across the λ_{max} sphere. For inner points in each shell defined by the internal surface, the numbers i of inaccessible orders are also shown in Fig. 4(*b*).

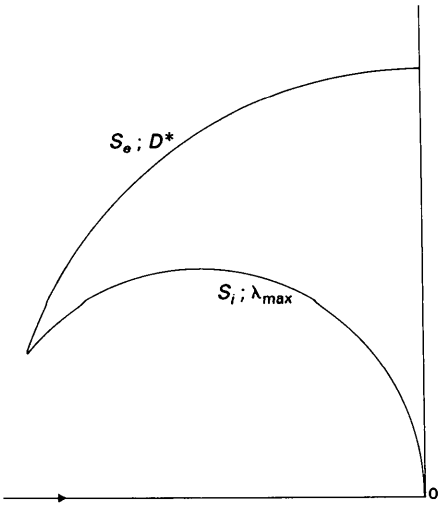

Fig. 3. The upper section of the volume of revolution for arbitrary D^* and λ_{max} but with zero λ_{min}. The external surface S_e is defined only by the D^* sphere and the internal surface by the λ_{max} sphere.

Fig. 4(*c*) combines the nests of the external and internal surfaces. The multiplicities m for the subregions shown in Fig. 4(*c*) are obtained by subtracting the inaccessible multiplicities i of Fig. 4(*b*) from the multiplicities n of Fig. 4(*a*).

We define $V(n, m)$ as the volume of the subregion whose inner points generate rays with recorded multiplicity m and maximum harmonic of order n. Subregions $V(1,1)$; $V(2,1)$, $V(2,2)$; $V(3,1)$, $V(3,2)$, $V(3,3)$; ... are shown in Fig. 4(*d*). Only the volumes $V(1,1)$, $V(2,2)$, $V(3,3)$, ... are in the experimentally accessible region of reciprocal space. For example, all rays with inner points in $V(3,3)$ emerge through the outer surface as triple rays. Inner points in $V(3,2)$ are outside the accessible region, but their second- and third-order points are accessible, so they generate double rays. Inner points in $V(3,1)$ are also outside the accessible region, as are their second-order points, so their rays emerge through S_e as single rays.

Our task is now to determine the volume $V(n, m)$ of each subregion. It is known (Moffat *et al.*, 1986) that the volume of a region of revolution bounded by spheres of radii d^*, $1/\lambda_2$, $1/\lambda_1$, centred as in our problem, is $(\pi/4)d^{*4}(\lambda_2 - \lambda_1)$ for $\lambda_2 < 2/D^*$. For each subregion in Fig. 4(*d*), the λ boundaries are defined by $\lambda_2 = (n - m + 1)\lambda_{max}$ and $\lambda_1 = (n - m)\lambda_{max}$, so that $\lambda_2 - \lambda_1 = \lambda_{max}$, which is independent of n and m. The volumes $V(n, m)$ may then be obtained from the difference in volume between solids with the D^*/n and $D^*/(n+1)$ spheres as their d^* boundaries. If one defines the common factor $(\pi/4)D^{*4}\lambda_{max} = C$, the volumes of the subregions are therefore

$$V(1,1) = (1 - 1/2^4)C,$$
$$V(2,1) = V(2,2) = (1/2^4 - 1/3^4)C,$$
$$V(3,1) = V(3,2) = V(3,3) = (1/3^4 - 1/4^4)C.$$

The total volume of the accessible region is $V_R = (\pi/4)D^{*4}\lambda_{max} = C$, or indirectly $V_R = \sum_n V(n, n) = C$.

The volume generating single rays is

$$V(1) = \sum_n V(n, 1) = C.$$

Hence the proportion $p(1)$ of RLPs which lie on single rays is

$$p(1) = \frac{V(1)Q}{V^*}\frac{V^*}{V_R} = CQ/C = Q = 0{\cdot}832,$$

where Q is the probability of any RLP being an inner point (§ 2).

The volume generating the inner points of double rays is

$$V(2) = \sum_{n \geq 2} V(n, 2) = C/2^4,$$

so the proportion $p(2)$ of RLPs which lie on double rays is

$$p(2) = 2V(2)Q/V_R = Q/2^3 = 0{\cdot}104.$$

In general the proportion $p(m)$ of RLPs on m-tuple rays is

$$p(m) = mV(m)Q/V_R = Q/m^3.$$

The number of single rays is $p(1)N = QN$, and the total number of Laue reflections of rays of all multiplicities is

$$\sum_m [p(m)/m]N = QN(1+1/2^4+1/3^4+\ldots)$$

$$= QN\zeta(4) = 0{\cdot}904N,$$

where N is the total number of RLPs in the accessible region and $\zeta(4) = \pi^4/90$. The multiplicity distributions with respect to RLPs and rays are summarized in Table 2. A remarkable feature about these distributions is that they do not depend on the values of D^* and λ_{max} (provided $\lambda_{max} < 2/D^*$). This is because all the ratios $V(n, m)/V_R$ are independent of D^* and λ_{max}.

In the present model the proportion of RLPs which lie on single rays is 83·2%, whereas in the solid-sphere model of § 3 the proportion was 72·8%. The higher proportion is due to the possibility of rays emerging across S_e with multiplicities lower than the order of

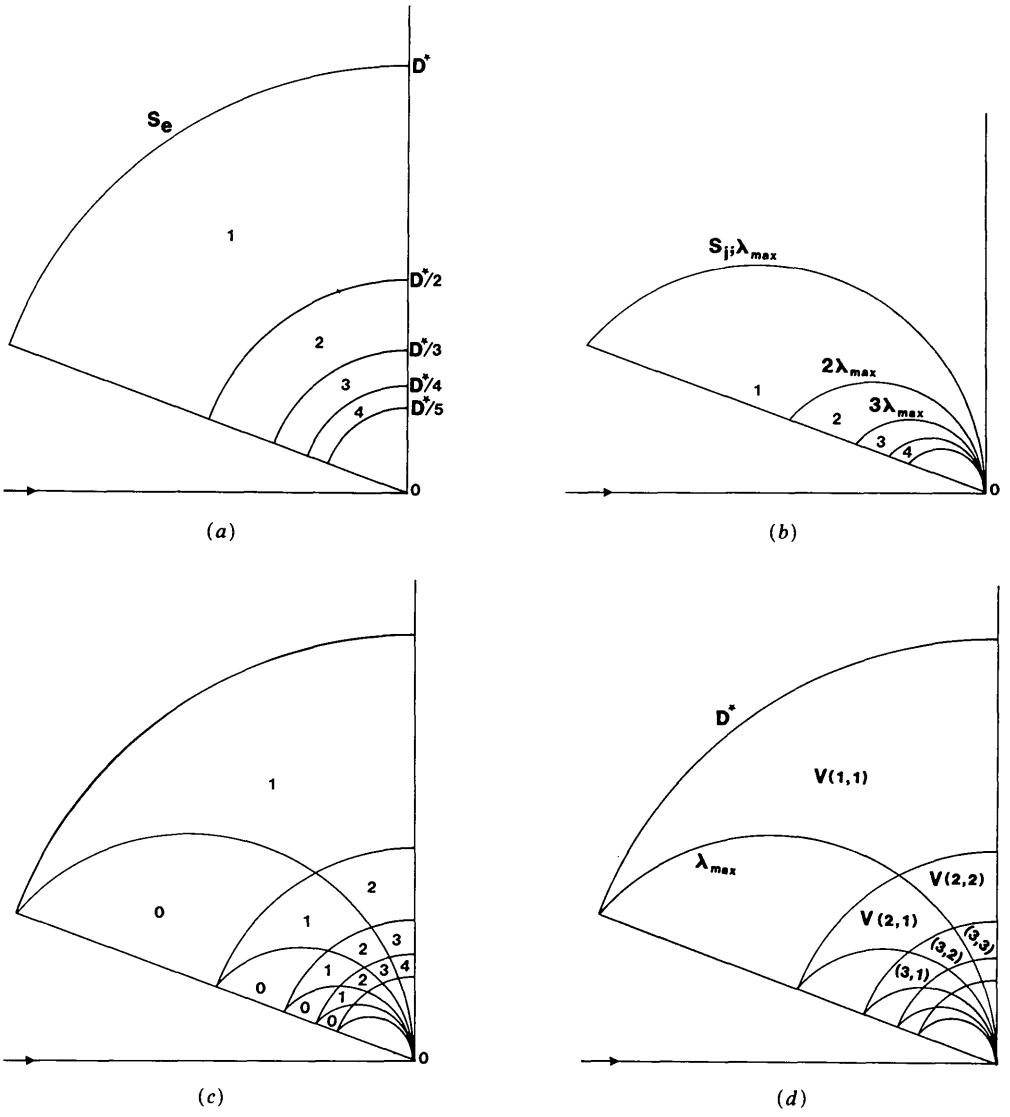

Fig. 4. Derivation of the observed multiplicities for the zero λ_{min} case. (*a*) The region defined by S_e is divided into shells separated by segments of spheres of radii $D^*/2$, $D^*/3$ *etc.* as in Fig. 2. The numbers in each shell refer to the multiplicities n of rays having their inner points in that shell. (*b*) The internal surface S_i defined by the λ_{max} sphere generates a family of surfaces of radii $1/n\lambda_{max}$ with $n = 2, 3, \ldots$ *etc.* The values shown are the number of inaccessible orders i for rays with inner points in each region. (*c*) This diagram combines the nests of the external and internal surfaces. The multiplicities m of the subregions are obtained by subtracting the inaccessible multiplicities i of (*b*) from the multiplicities n of (*a*). (*d*) This is identical to (*c*) but the subregions are now labelled with the appropriate volume labels $V(n, m)$.

Table 2. *Multiplicity distribution when* $\lambda_{min}=0$ *and* $\lambda_{max}<2/D^*$

Distribution of RLPs		Distribution of rays	
RLP on single rays	83·2%	Single rays	92·4%
RLP on double rays	10·4	Double rays	5·8
RLP on triple rays	3·1	Triple rays	1·1
RLP on quadruple rays	1·3	Quadruple rays	0·4
RLP on higher-order rays	2·0	Higher-order rays	0·3
	100·0		100·0

their highest harmonics, *e.g.* rays with inner points in $V(n, 1)$ have $(n-1)$ inaccessible RLPs and emerge only as single rays. Since the total number of accessible RLPs here is $N=(\pi/4)D^{*4}\lambda_{max}/V^*$, the actual number of rays of a given multiplicity is dependent on λ_{max} and V^*, and very strongly dependent on D^*.

5. Model for arbitrary D^*, λ_{max} and λ_{min}

The same principles can now be applied to the more general case of arbitrary λ_{max} (where $\lambda_{max}<2/D^*$) and λ_{min}. Again the boundary surface of the accessible region is divided into an external surface S_e and an internal surface S_i. Fig. 5(*a*) shows the nest of shells defined by the external surface. The external surface itself now has two segments, one from the D^* sphere and one from the λ_{min} sphere. Its successive nesting inner surfaces $S_{e2}, S_{e3}, \ldots, S_{en}, \ldots$ are each made of parts of spheres of radii D^*/n and $1/n\lambda_{min}$. Apart from the changed shape of the nest of external surfaces the approach is similar to the $\lambda_{min}=0$ case (§ 4 and Fig. 4). The nest of internal surfaces in Fig. 5(*b*) is unaltered, and Fig. 5(*c*) combines the nests of the external and internal surfaces. Again the multiplicities

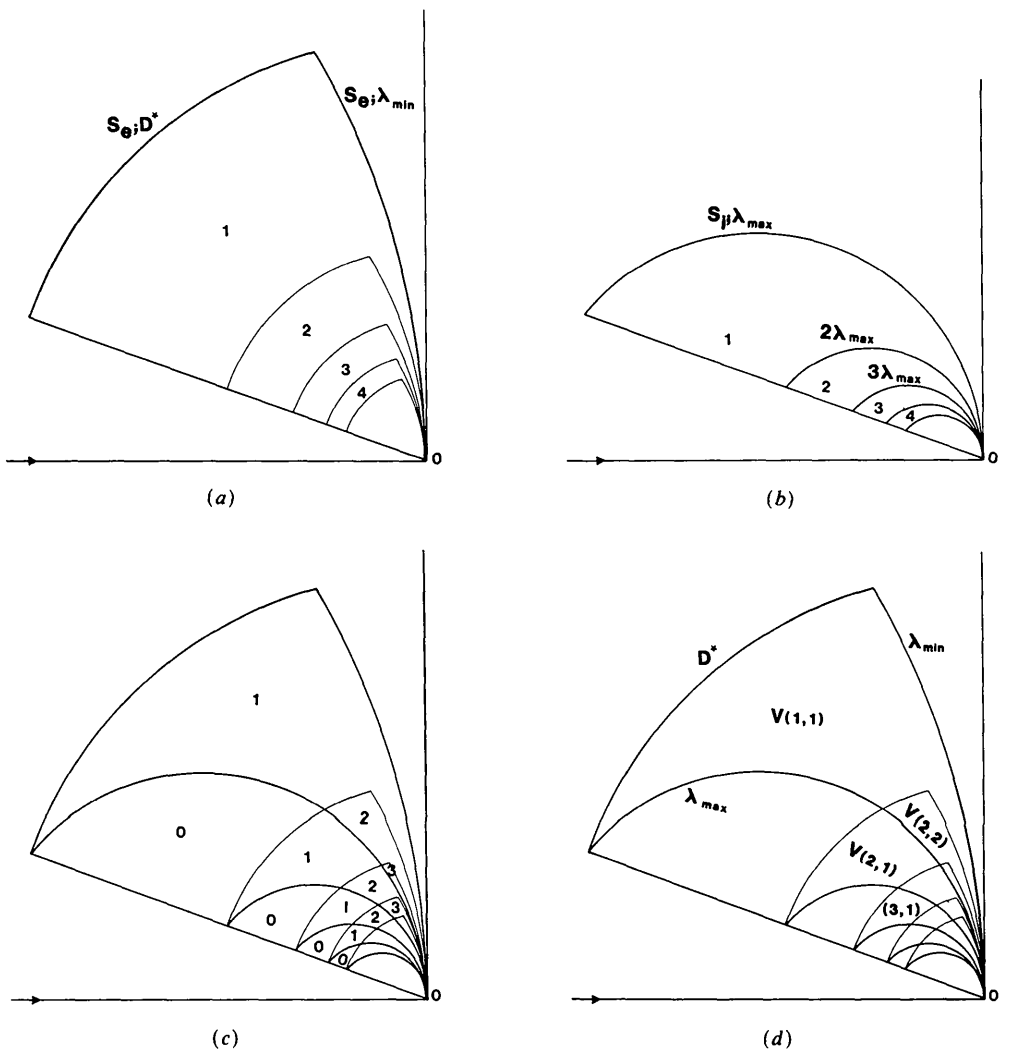

Fig. 5. Diagrams for the general case of arbitrary D^*, λ_{max} and λ_{min}. (*a*) The nest of shells defined by the external surface with the values of n shown in each region. (*b*) The nest of internal surfaces associated with λ_{max} and the values of the inaccessible multiplicities i. (*c*) The multiplicities m of rays equal $(n-i)$ and are the values labelling each region. (*d*) The subregions are labelled with their associated volumes $V(n, m)$.

m of rays passing through RLPs in the accessible region are found by subtracting the inaccessible multiplicities i of Fig. 5(b) from the multiplicities n of Fig. 5(c). The subregions, Fig. 5(d), are labelled $V(n, m)$ as before, where m denotes the recorded multiplicity of an emerging ray whose maximum harmonic is of order n. However, the formulae for the $V(n, m)$ are now considerably more complicated because of the possible interleaving of the $n\lambda_{\min}$ and $(n+1)\lambda_{\min}$ spheres between the $\lambda_{\max}$, $2\lambda_{\max}$, ... and $n\lambda_{\max}$ spheres.

Let M denote the ratio $\lambda_{\max}/\lambda_{\min}$. Fig. 6 illustrates a set of subregions $V(n, 1)$, $V(n, 2)$, ... in more detail for arbitrary values of n and M. The nest boundaries S_{en} and $S_{e(n+1)}$ defined from the external surface are segments of the spheres D^*/n and $n\lambda_{\min}$, and $D^*/(n+1)$ and $(n+1)\lambda_{\min}$. The relevant array of nests defined from the internal surface are parts of the spheres $\lambda_{\max}$, $2\lambda_{\max}$, ..., $n\lambda_{\max}$. Clearly if the $\lambda_{\max}$ sphere lies to the right of the $n\lambda_{\min}$ sphere, $V(n, n)=0$. This occurs for $n>M$. More generally $V(n, n-i)=0$ when $n>(i+1)M$.

For volumes represented on the left side of Fig. 6, $V(n, m)$ retains the same formula as in the $\lambda_{\min}=0$ case, so long as the $(n-m)\lambda_{\max}$ sphere lies to the left of the $(n+1)\lambda_{\min}$ sphere, *i.e.* when $(n-m)\lambda_{\max}>(n+1)\lambda_{\min}$ or $(n-m)M>(n+1)$.

We are now ready for the general calculation of $V(n, 1)$ and $V(n, m)$ leading to formulae for $p(1)$ and $p(m)$.

Single rays. If we put $(\pi/4)D^{*4}\lambda_{\min}=K$, then from the discussion of Fig. 6

$$V(n, 1)/K = A_{n,1}/n^4 - B_{n,1}/(n+1)^4,$$

where

$$A_{n,1} = nM - \max[(n-1)M, n]$$

$$B_{n,1} = nM - \max[(n-1)M, \min\{(n+1), nM\}].$$

By reference to Fig. 6, we see that $A_{n,1}$ is related to the wavelength change along the upper segment from the D^*/n sphere, and $B_{n,1}$ is related to the wavelength change along the lower segment (if any) from the $D^*/(n+1)$ sphere.

On manipulation

$$A_{n,1} = \begin{cases} M & \text{if } M \geq n/(n-1) \\ n(M-1) & \text{if } M \leq n/(n-1), \end{cases}$$

$$B_{n,1} = \begin{cases} M & \text{if } M \geq (n+1)/(n-1) \\ n(M-1)-1 & \text{if } (n+1)/(n-1) \\ & \quad \geq M \geq (n+1)/n \\ 0 & \text{if } M \leq (n+1)/n. \end{cases}$$

Evidently $V(1)=\sum_n V(n, 1)$ is a series in $1/n^4$. We therefore collect the terms in $1/n^4$ from $V(n-1, 1)$ and $V(n, 1)$. The coefficient of $1/n^4$ in $V(1)/K$ is then $C_{n,1}=-B_{n-1,1}+A_{n,1}$ where

$$C_{n,1} = \begin{cases} 0 & \text{if } M \geq n/(n-2) \\ n-(n-2)M & \text{if } n/(n-2) \geq M \geq n/(n-1) \\ n(M-1) & \text{if } M \leq n/(n-1). \end{cases}$$

The values of the first three coefficients are

$$C_{1,1} = M-1,$$

$$C_{2,1} = \begin{cases} 2 & \text{if } M \geq 2 \\ 2(M-1) & \text{if } M \leq 2, \end{cases}$$

$$C_{3,1} = \begin{cases} 0 & \text{if } M \geq 3 \\ 3-M & \text{if } 3 \geq M \geq 3/2 \\ 3(M-1) & \text{if } M \leq 3/2. \end{cases}$$

The volumes generating singles $V(1)=K\sum_n C_{n,1}/n^4$ are thus given by

if $M \geq 3$, $V(1)/K = (M-1)/1^4 + 2/2^4$,

if $3 \geq M \geq 2$, $V(1)/K = (M-1)/1^4 + 2/2^4 + (3-M)/3^4$,

if $2 \geq M \geq 5/3$, $V(1)/K = (M-1)/1^4 + 2(M-1)/2^4 + (3-M)/3^4 + (4-2M)/4^4$

etc. Evidently the smaller is M the longer is the series. Since $C_{n,1}=0$ when $M \geq n/(n-2)$, all $C_{n,1}$ vanish when $n \geq 2M/(M-1)$.

The total volume of the accessible region defined by the D^*, $\lambda_{\max}$, $\lambda_{\min}$ spheres is

$$V_R = (\pi/4)D^{*4}(\lambda_{\max}-\lambda_{\min}) = K(M-1).$$

As previously, the proportion of RLPs which lie on single rays is

$$p(1) = V(1)Q/V_R,$$

so that when $M \geq 3$

$$p(1) = [(M-1)+1/2^3]Q/(M-1).$$

When $M \to \infty$, $p(1) \to Q = 0{\cdot}832$ in agreement with the earlier treatment for $\lambda_{\min}=0$ (§ 4).

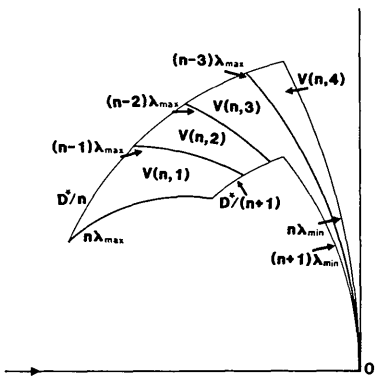

Fig. 6. A set of subregions $V(n, 1)$, $V(n, 2)$ *etc.* of Fig. 5(d) is shown suitably expanded for clarity.

The behaviour of $p(1)$ as a function of $M = \lambda_{max}/\lambda_{min}$ is shown in Fig. 7. A very important point to notice is that $p(1)$ does not depend on D^* (provided $\lambda_{max} < 2/D^*$); it depends only on M. $p(1)$ rises from 83·2% at large M to 88·4% at $M = 3$, to 94·6% at $M = 2$, to 97·4% at $M = 1{\cdot}5$, and tends to 100% as M tends towards 1·0. Note that there are discontinuities in the slope of the curve at $M = 3$, 2, 5/3, 3/2, 7/5, 4/3, ... The slope discontinuity is especially marked at $M = 2$, as can be appreciated from the expressions for $V(1)$ given above.

A further comment may be made about the case when the incident radiation has a narrow wavelength range with $M < 2$. It follows directly from the ratio of λ_{max} to λ_{min} and the ratio of the reciprocal radii of successive orders along a ray that any accessible RLP of order less than $1/(M-1)$ will lie on a single ray. Thus if, say, $M = 1{\cdot}9$, all accessible first-order RLPs will lie on single rays. If $M = 1{\cdot}45$ all accessible second- and first-order RLPs will lie on single rays, and if, say, $M = 1{\cdot}09$ all accessible RLPs of order 11 or less will lie on single rays.

Multiple rays. A similar examination of diagrams like Fig. 6 leads for the volumes generating the inner points of m-tuple rays to the results

$$V(n, m)/K = A_{n,m}/n^4 - B_{n,m}/(n+1)^4,$$

where

$$A_{n,m} = (n-m+1)M - \max[(n-m)M, \min\{n, (n-m+1)M\}],$$

$$B_{n,m} = (n-m+1)M - \max[(n-m)M, \min\{(n+1), (n-m+1)M\}].$$

$V(m) = \sum_{n \geq m} V(n, m)$ is a series in $1/n^4$, and we collect the terms in $1/n^4$ from $V(n-1, m)$ and $V(n, m)$. The contributions $-B_{n-1,m}$ and $A_{n,m}$ to the coefficients $C_{n,m}$ of $1/n^4$ in $V(m)/K$ for various ranges of value of M are set out in Table 3. As particular examples

$$C_{2,2} = \begin{cases} M-2 & \text{if } M \geq 2 \\ 0 & \text{if } M \leq 2, \end{cases}$$

$$C_{5,3} = \begin{cases} 0 & \text{if } M \geq 5 \\ 5-M & \text{if } 5 \geq M \geq 5/2 \\ 3M-5 & \text{if } 5/2 \geq M \geq 5/3 \\ 0 & \text{if } M \leq 5/3. \end{cases}$$

The volumes generating doubles are thus

if $M \geq 4$ $\quad V(2)/K = (M-2)/2^4 + 3/3^4$,

if $4 \geq M \geq 3$ $\quad V(2)/K = (M-2)/2^4 + 3/3^4 + (4-M)/4^4$,

if $3 \geq M \geq 5/2$ $\quad V(2)/K = (M-2)/2^4 + (2M-3)/3^4 + (4-M)/4^4$

etc. The volumes generating triples are

if $M \geq 5$ $\quad V(3)/K = (M-3)/3^4 + 4/4^4$,

if $5 \geq M \geq 4$ $\quad V(3)/K = (M-3)/3^4 + 4/4^4 + (5-M)/5^4$,

if $4 \geq M \geq 3$ $\quad V(3)/K = (M-3)/3^4 + (2M-4)/4^4 + (5-M)/5^4$,

if $3 \geq M \geq 5/2$ $\quad V(3)/K = (2M-4)/4^4 + (5-M)/5^4 + (6-2M)/6^4$

etc. Again, the smaller is M, the longer is the series.

From Table 3, $C_{n,m} = 0$ for $M \geq n/(n-m-1)$, so that all $C_{n,m}$ vanish for $n \geq (m+1)M/(M-1)$. However $C_{n,m} = 0$ also for $M \leq n/(n-m+1)$, so that early terms in the series when $m \geq 2$ also drop out as M decreases.

The proportion of RLPs which lie on m-tuple rays is

$$p(m) = mV(m)Q/V_R,$$

where $V_R = K(M-1)$. Curves for $p(2)$ and $p(3)$ as functions of M are also shown in Fig. 7. $p(2)$ falls slowly from 10·4% at large M ($\lambda_{min} = 0$) to 8·6% at $M = 3$, and then rapidly to 3·6% at $M = 2$, to 1·8% at $M = 3/2$ and towards zero as M tends to 1·0. $p(2)$ has slope discontinuities at $M = 4$, 3, 5/2, 2, 7/4, ... $p(3)$ falls from 3·1% at large M to 2·5% at $M = 4$,

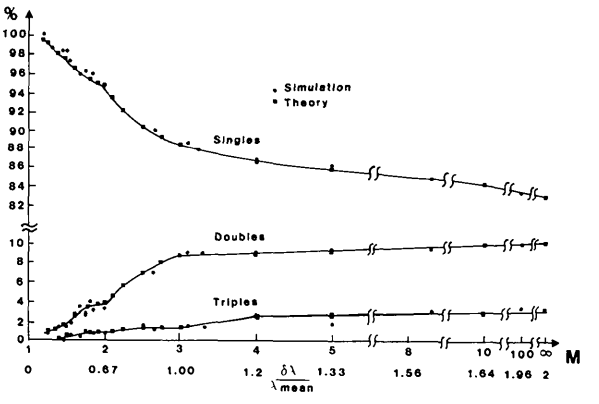

Fig. 7. The variation with M of the proportions $p(1)$, $p(2)$ and $p(3)$ of RLPs lying on single, double and triple rays. The value of $\lambda_{max} < 2/D^*$. The points marked • are the results from computer simulations; the parameters for these were $D^*_{max} = (2{\cdot}5\ \text{Å})^{-1}$, cubic space group, 50 Å primitive cell in a general orientation, spindle 15°, $\varphi_x = 5$, $\varphi_y = -28$, $\varphi_z = -80{\cdot}2°$. The crystal-to-film distance was +2 mm (for $\lambda_{max} < 2/\sqrt{2}D^*$) but for $2/\sqrt{2}D^* < \lambda_{max} < 2/D^*$ two simulations were added together (forward- and backscattering) to give an almost complete count of rays.

Table 3. *Coefficients of* $1/n^4$ *contributing to* $V(m)/K$

	$M > \frac{n}{n-m-1}$	$\frac{n}{n-m-1} > M > \frac{n}{n-m}$	$\frac{n}{n-m} > M > \frac{n}{n-m+1}$	$M < \frac{n}{n-m+1}$
$-B_{n-1,m}$	$-M$	$-(n-m)M+n$	0	0
$A_{n,m}$	M	M	$(n-m+1)M-n$	0
$C_{n,m}=-B_{n-1,m}-A_{n,m}$	0	$n-(n-m-1)M$	$(n-m+1)M-n$	0

to 1·4% at $M=3$ and to 0·4% at $M=3/2$. It has slope discontinuities at $M=5, 4, 3, 5/2, 7/3, \ldots$.

6. Model for $\lambda_{max} > 2/D^*$

All previous sections assumed that $\lambda_{max} < 2/D^*$ or, equivalently, that the maximum scattering angle 2θ was less than π. For macromolecular crystals this is an experimentally reasonable assumption. Even the most highly ordered protein crystals have $D^* \leq 1{\cdot}0$ Å^{-1}. However, for crystals of inorganic and small organic molecules, larger values of D^* are common. Although all Laue synchrotron experiments to date have used values of $\lambda_{max} \leq 2{\cdot}6$ Å, future experiments may require substantially larger values of λ_{max}, for example to stimulate the K edges of calcium or sulfur at 3 and 5 Å respectively. Thus, for completeness, we now relax the prior condition that $\lambda_{max} < 2/D^*$, and further assume that data for all scattering angles, $0 < 2\theta \leq \pi$, are recorded by the detector.

The situation is shown in Fig. 8, which is directly modelled on Fig. 4 and with which it should be compared. The subregions $V(n, m)$ in Fig. 8 again are those for which an emerging ray is of multiplicity m, with a maximum harmonic of order n. The volumes of these subregions may be calculated analytically, to yield as before the fraction of all rays of multiplicity m. Rather than present the analytical results we show in Fig. 9 the results of an extensive computer simulation, in which λ_{max} was varied between 5 Å (*i.e.* $2/D^*$) and 100 Å, for λ_{min} values of 0·025, 0·5 and 1·0 Å. For $\lambda_{max} = 5$ Å, the three data points agree with the corresponding points of Fig. 7 and, in particular, the proportion of single reflections for $\lambda_{min} = 0{\cdot}025$ Å (which is effectively 0 Å) is 83·2%, the analytical result (§ 4). For the largest values of λ_{max}, the proportion of singles is 73·2% for all values of λ_{min}, the analytical result for infinite wavelength range (§ 3). The computer-simulated curves between these two limiting proportions appear smooth; the discontinuities in slope which the analytical treatment shows to be present are so slight as to be undetectable, in contrast with the case when $\lambda_{max} < 2/D^*$ shown in Fig. 7. Note that here there is a different curve for each value of λ_{min}. That is, the proportion of singles now depends on two variables separately, $\lambda_{max}D^*$ and $\lambda_{min}D^*$, and not merely on the single variable $\lambda_{max}/\lambda_{min}$, as in the case when $\lambda_{max} < 2/D^*$.

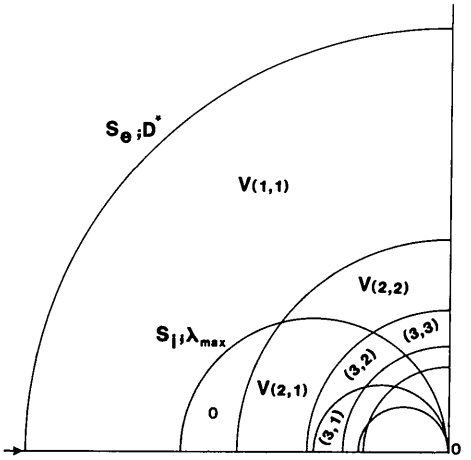

Fig. 8. The multiplicities for the case when $\lambda_{max} > 2/D^*$. This diagram is modelled on Fig. 4. As previously, $V(n, m)$ is the volume of the subregion whose inner points generate rays with recorded multiplicity m and maximum harmonic of order n.

7. Total number of single and double reflections

Figs. 7 and 9 show that, as the wavelength range increases, the fraction of single reflections decreases monotonically. However, an increase in the wavelength range results in an exactly proportional increase in the total number of reciprocal-lattice points that are stimulated (Moffat *et al.*, 1986), provided $\lambda_{max} < 2/D^*$. The total number of single reflections, and of doubles and higher multiples, may then increase also. With present experimental methods, quantification of structure amplitudes from Laue reflections is sufficiently precise for single and double

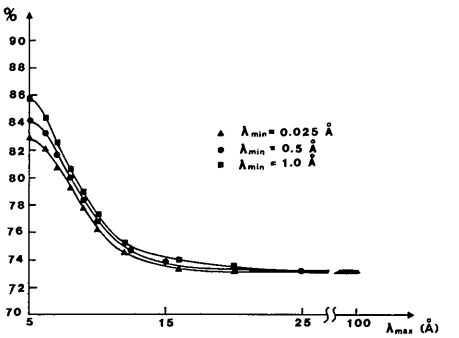

Fig. 9. Model for $\lambda_{max} > 2/D^*$. The variation of the proportion $p(1)$ of singles with λ_{max} for three different values of λ_{min}. For $\lambda_{max} = 5$ Å the three data points shown agree with the points on the curve in Fig. 7 (M values of 5, 10, 200). (The simulation parameters are as given in the caption to Fig. 7.)

reflections (Zurek *et al.*, 1985), but not so for triple and higher multiples. The total number of quantifiable structure amplitudes from a Laue data set is then the total number of singles, or of singles plus doubles.

Fig. 10 shows the form of the variation of the total number of all reflections, the total number of singles, and the total number of doubles, as a function of λ_{max} for fixed D^*. The total number of all reflections N_T is given by

$$N_T = \pi D^{*4}(\lambda_{max} - \lambda_{min})/4V^* \text{ for } \lambda_{max} < 2/D^*$$

and

$$N_T = \pi D^{*3}(8 - 3\lambda_{min}D^*)/12V^* - 4\pi/3\lambda_{max}^3 V^* \text{ for } \lambda_{max} > 2/D^*,$$

which tends to the constant value

$$N_T = \pi D^{*3}(8 - 3\lambda_{min}D^*)/12V^*$$

as λ_{max} becomes large.

The curve for the total number of singles has four sections. For $\lambda_{max} \geq 6/D^*$, the number of singles is constant and given by $7QD^{*3}/12V^*$ (for $\lambda_{min} = 0$). For $2/D^* \leq \lambda_{max} < 6/D^*$, the curve passes through a broad shallow maximum at $\lambda_{max} \simeq 3{\cdot}4/D^*$. For $3\lambda_{min} \leq \lambda_{max} < 2/D^*$, the curve is exactly linear with a slope S_1 of $\pi D^{*4}Q/4V^*$ and an intercept on the λ_{max} axis of $7/8\lambda_{min}$. For $\lambda_{min} < \lambda_{max} \leq 3\lambda_{min}$, the curve is an array of linear segments with discontinuities of slope at $\lambda_{max} = 3\lambda_{min}$, $2\lambda_{min}$, $5/3\lambda_{min}$, $3/2\lambda_{min}, \ldots$, corresponding to the points of discontinuity in Fig. 7. Although the slope of each segment differs (and may be readily calculated from the equations in § 5), the segments do not deviate appreciably from the line of slope S_1. For most practical purposes the curve may be approximated as linear for $\lambda_{min} < \lambda_{max} < 2/D^*$. That is, the total number of single reflections, like the total number of all reflections, is proportional to the wavelength range $(\lambda_{max} - \lambda_{min})$ for $\lambda_{max} < 2/D^*$.

The curve for the total number of doubles has a broadly similar form. Linear segments extend up to $\lambda_{max} = 2/D^*$, followed by a broad shallow maximum at $\lambda_{max} \simeq 5/D^*$ and a constant region for $\lambda_{max} \geq 8/D^*$. Again, for most practical purposes the curve may be approximated as linear for $\lambda_{min} < \lambda_{max} < 2/D^*$. Thus the curve for singles plus doubles may also be approximated as linear over this range.

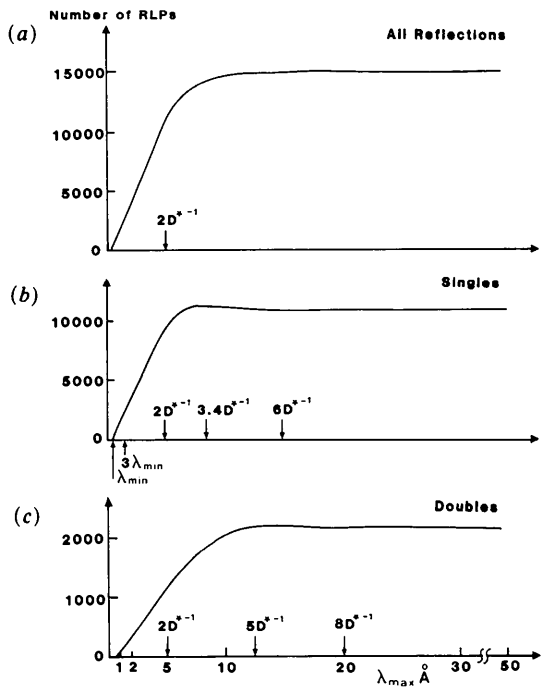

Fig. 10. The variation of the numbers of RLPs as a function of λ_{max}. (*a*) Total number of all reflections; (*b*) total number of singles; (*c*) total number of RLPs lying on double rays. (λ_{min} = 0·5 Å, other simulation parameters as given in the caption to Fig. 7.)

8. Dependence of the distributions on d^* and θ

8.1. *Mosaics*

The previous sections have presented results for the total numbers and proportions of rays which are singles, doubles *etc.* We now wish to find as a function of position in V_R the probability distributions for RLPs lying on single, double, triple *etc.* rays. For simplicity we consider only cases with $\lambda_{max} < 2/D^*$, and thus return to the analysis of § 5.

To find these probability distributions we combine two ideas introduced above: the $V(n, m)$ are the regions whose first-order points generate rays with maximum order n and multiplicity m within V_R (§ 4); and in any region of reciprocal space the probability of a randomly chosen RLP being a first-order point is Q (= 0·832), of being a second-order point is $Q/2^3$ (= 0·104), of being a third-order point is $Q/3^3$ (= 0·031) *etc.* (§ 3).

For given n, m the rays generated from first-order points in $V(n, m)$ have their jth-order points in a region $U(n, m, j)$ obtained by a linear scaling of $V(n, m)$ outwards from the origin by a factor j. The ratio of volumes is $U(n, m, j) = j^3 V(n, m)$. For a jth-order point to lie in the accessible region V_R, j must satisfy $(n - m + 1) \leq j \leq n$. With this restriction on j all the $U(n, m, j)$ lie within V_R.

For every order j, we can partition V_R into a mosaic, made up of a series of regions $U(n, m, j)$, such that a RLP of order j lying within the region has its first order lying within $V(n, m)$. In the case discussed in § 5, V_R is bounded by the D^*, λ_{max} and λ_{min} spheres. For given j the corresponding set of first-order regions $V(n, m)$ is bounded by the D^*/j, $j\lambda_{max}$ and $j\lambda_{min}$ spheres.

The process may be understood by an example. For specified D^*, λ_{max} and λ_{min}, with say $M \geq 4$, we draw the $V(n, m)$ regions as in Fig. 11(*a*). The integers

within the boundaries show the multiplicity m associated with each region. The first-order points within V_R are then categorized directly by the $V(n, m)$ since $U(n, m, 1) = V(n, m)$. However, only the $V(n, n) = U(n, n, 1)$ lie within V_R, so the distribution of multiplicities associated with first-order points shown in Fig. 11(b) is simply a copy of part of Fig. 11(a).

The multiplicity classification of second-order points within V_R is obtained from Fig. 11(a) by taking the $V(n, m)$ within the region bounded by the $D^*/2$, $2\lambda_{max}$ and $2\lambda_{min}$ spheres, and scaling up the diagram by a factor two to obtain the $U(n, m, 2)$. The resulting mosaic is shown in Fig. 11(c). Any second-order RLP lying, say, in the region $U(4, 3, 2)$ belongs to a ray

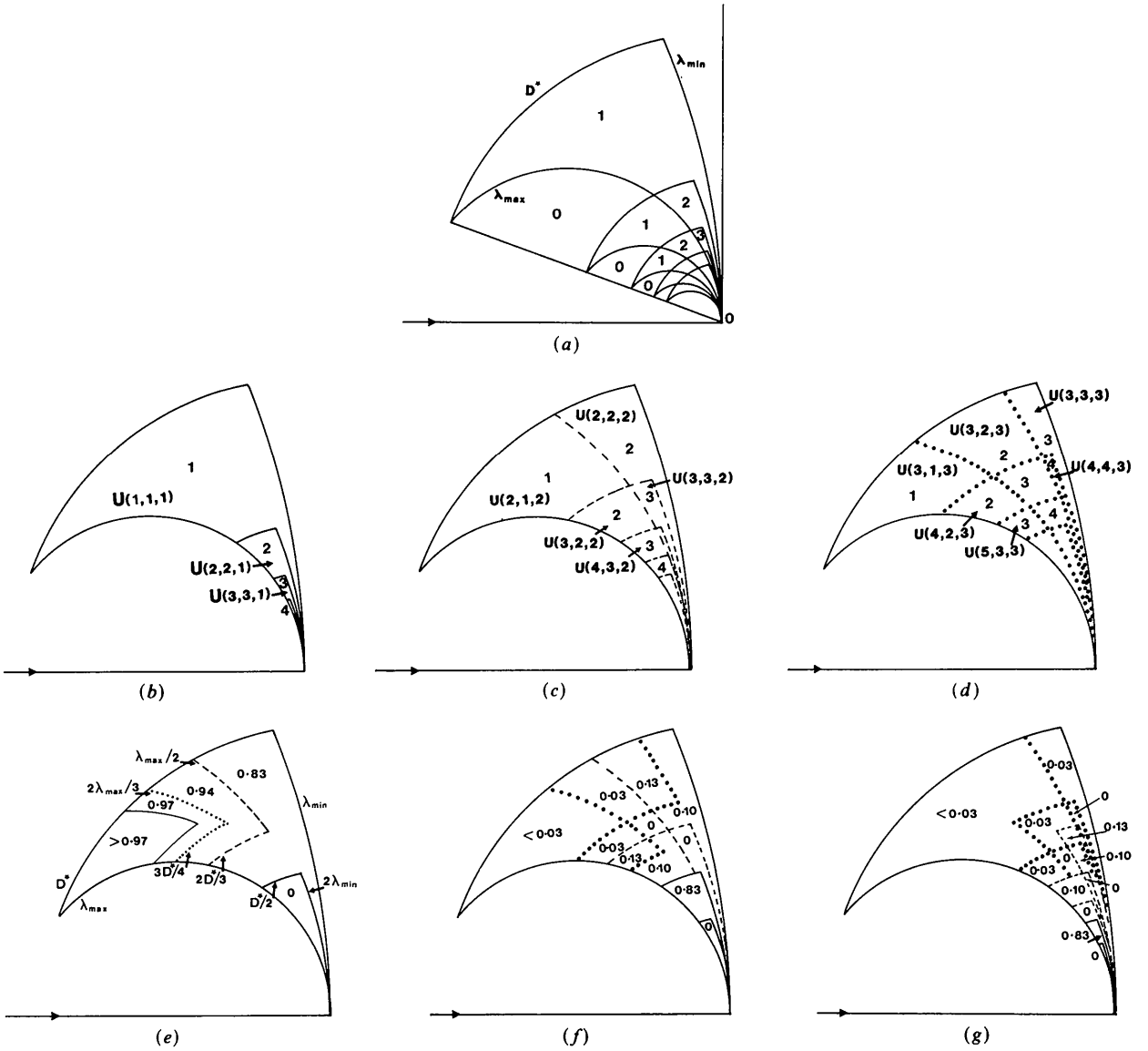

Fig. 11. Dependence of the distributions on d^* and θ. (The value of M used in the diagrams lies in the range $4 < M < 5$, which is a reasonable general case.) (a) The $V(n, m)$ regions with their multiplicities shown. (b) The Q mosaic or distribution of multiplicities associated with first-order points within V_R [*i.e.* the $U(n, n, 1)$]. This is a copy of part of (a). (c) The $Q/2^3$ mosaic or multiplicity classification of second-order points within V_R [*i.e.* the $U(n, m, 2)$]. Note that the region of interest from (a) between $D^*/2$, $2\lambda_{max}$ and $2\lambda_{min}$ has been scaled up by a factor of two here. (d) The $Q/3^3$ mosaic or multiplicity classification of third-order points within V_R [*i.e.* the $U(n, m, 3)$]. The appropriate part of (a) has been scaled up by a factor of three here. (e) The probability distribution for singles is obtained by superposing the appropriate regions of (b), (c), (d). The probability of a RLP being single is marked for each new region. For clarity the successive overlap of regions into the top left-hand corner of V_R has been omitted. (f) The probability distribution for doubles is obtained by selecting the regions of multiplicity 2 from (b), (c), (d). For clarity only the five most important regions have been selected. The probabilities which result are marked. (g) The probability distribution for triples is built up in the same way as for the singles and doubles in (e), (f). The region of highest probability is $U(3, 3, 1)$. For clarity only a few of the triple regions are shown.

of multiplicity 3 as indicated in the figure. Fig. 11(*d*) shows the multiplicity classification of third-order points obtained by enlarging the appropriate part of Fig. 11(*a*) by a factor three. Higher-order mosaics may be similarly obtained.

8.2. *Probability distributions*

We now turn to probability distributions, and find first how the probability that a randomly selected RLP lies on a single ray varies with position inside V_R.

The probability that a randomly chosen RLP is first order is Q. Thus the first-order mosaic, Fig. 11(*b*), may be called the Q mosaic. Its partitions show the multiplicities of the rays associated with first-order RLPs in the different regions. Likewise, the second-order mosaic, Fig. 11(*c*), with probability $Q/2^3$ for a second-order point, may be called the $Q/2^3$ mosaic, and its partitions show the multiplicities of rays associated with second-order RLPs in the different regions. Similarly, the Q/j^3 mosaic would show multiplicities associated with jth-order points.

In the Q mosaic first-order points will be singles only when the RLP is in the region $U(1, 1, 1)$; elsewhere the probability of a first-order RLP lying on a single ray will be zero. In the $Q/2^3$ mosaic second-order points will lie on single rays only when the RLP is in the region $U(2, 1, 2)$. Thus the probability distribution for singles can be obtained by superimposing $U(1, 1, 1)$ with probability Q, $U(2, 1, 2)$ with probability $Q/2^3$, $U(3, 1, 3)$ with probability $Q/3^3$ *etc.* The result of this superposition is shown in Fig. 11(*e*).

The diagram has a particularly simple form, since as n increases each $U(n, 1, n)$ covers a smaller part of V_R than its predecessor, and they all reach into the top left-hand corner. Thus the probability distribution is built up from a series of layers with probability weights Q/j^3. Since $Q(1+1/2^3+1/3^3+\ldots)=1$, the probability of a RLP lying on a single ray is very nearly 1 for any RLP selected near to the top left-hand corner of V_R. The probability reduces gradually to $Q(1+1/2^3)=0{\cdot}936$ in the region with $(3/4)D^* > d^* > (2/3)D^*$ and $(2/3)\lambda_{max} > \lambda > (1/2)\lambda_{max}$. The probability is $Q=0{\cdot}832$ in the large region unique to $U(1, 1, 1)$, but it falls to zero in the region where $d^* < D^*/2$ and $\lambda > 2\lambda_{min}$. In this region there are no RLPs which lie on single rays.

The set of diagrams in Fig. 11 has been drawn for $4 \le M \le 5$. The general features of the singles distribution shown in Fig. 11(*e*) are correct also for $M \ge 3$. For $2 \le M \le 3$ $U(2, 1, 2)$ acquires a tail through low d^* stretching to the origin, as shown in Fig. 12. For $M \le 2$, $U(1, 1, 1)$ fills the accessible volume V_R, and other $U(n, 1, n)$ also acquire tails.

The probability distribution for doubles, that is the probability that a randomly chosen RLP lies on a double ray, is obtained by selecting the regions of multiplicity 2 from the Q, $Q/2^3$, $Q/3^3$ *etc.* mosaics (Figs. 11*b*, *c*, *d*). The resulting diagram for doubles does not have the visual simplicity of that for singles because the $U(n, 2, j)$ regions only partly overlap. For clarity only the five most important regions are shown in Fig. 11(*f*), *viz* $U(2, 2, 1)$ from the Q mosaic, $U(2, 2, 2)$ and $U(3, 2, 2)$ from the $Q/2^3$ mosaic and $U(3, 2, 3)$ and $U(4, 2, 3)$ from the $Q/3^3$ mosaic. $U(2, 2, 1)$, the highest-probability region, is not overlapped by any of the others, but there is partial overlap of $U(3, 2, 2)$ and $U(4, 2, 3)$ and of $U(2, 2, 2)$ and $U(3, 2, 3)$. As n increases the regions $U(n, 2, n-1)$ and $U(n, 2, n)$ diminish in probability, and their positions and partial overlaps are such that the probability of a random RLP lying on a double ray diminishes to zero near the (D^*, λ_{max}) left-hand top corner, as it must for consistency with the high probability there for singles.

The general features of Fig. 11(*f*) are correct for $M \ge 4$. For $M \le 4$, first $U(3, 2, 2)$ and $U(3, 2, 3)$ acquire tails stretching to the origin, and then also other $U(n, 2, j)$ as M further decreases.

The most important parts of the probability distribution for triples derived from Figs. 11(*b*), (*c*) and (*d*) are shown in Fig. 11(*g*). The region of highest-probability Q is $U(3, 3, 1)$.

8.3. *Combined distributions and coverage*

For the accurate measurement of X-ray intensities we are particularly concerned with single and double rays (and perhaps with triple rays as techniques improve). We need to know the extent to which their combined distributions provide a good coverage or sampling of the RLPs within V_R.

Since $Q=0{\cdot}832$, $Q/2^3=0{\cdot}104$ and $Q/3^3=0{\cdot}031$, it is clearly important to have good coverage of the first-order points in the Q mosaic. Singles provide sampling of the $U(1, 1, 1)$ region, but as remarked earlier there are no singles when $M > 2$ in the region

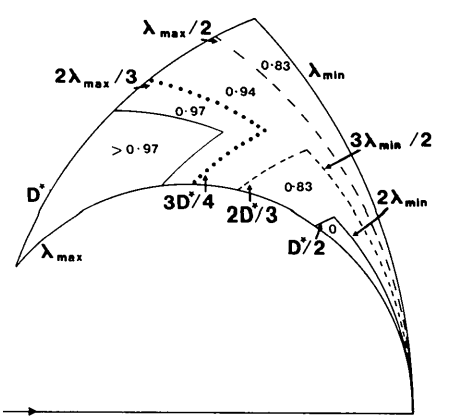

Fig. 12. For $2 < M < 3$ the region $U(2, 1, 2)$ acquires a tail through low d^* stretching to the origin. This should be contrasted with the shape of $U(2, 1, 2)$ in Fig. 11(*e*) for $4 < M < 5$.

Table 4. *Percentage coverage of RLPs as a function of* $M = \lambda_{max}/\lambda_{min}$

	Full range $d^* \le D^*$		$d^* \le D^*/2$		$d^* \le D^*/3$
M	Singles	Singles + doubles	Singles	Singles + doubles	Singles + doubles
$\infty(\lambda_{min}=0)$	83·2%	93·6%	0	66·8%	0
5	85·8	95·1	20·8	76·3	42·9
3	88·4	97·0	41·6	88·9	88·9
2	94·6	98·2	88·4	96·0	96·0

Table 5. *Numbers of RLPs as a function of* $M = \lambda_{max}/\lambda_{min}$

The calculations assume $D^* = 0{\cdot}5$ Å^{-1} with 10 000 RLPs in hemisphere. For $M = \infty$, $\lambda_{max} = 2.5$ Å and $\lambda_{min} = 0$. For $M = 5, 3, 2$, $\lambda_{min} = 0{\cdot}5$ Å.

	Full range $d^* \le D^*$			$d^* \le D^*/2$			$d^* \le D^*/3$	
M	Singles	Singles + doubles	Max. accessible	Singles	Singles + doubles	Max. accessible	Singles + doubles	Max. accessible
∞	3899	4387	4687	0	195	292	0	57
5	3217	3567	3750	48	178	234	19	46
3	1657	1818	1875	48	104	117	20	23
2	887	921	937	51	56	58	11	11
(Hemisphere)	—	—	(10 000)	—	—	(1250)	—	(370)

where $d^* < D^*/2$ and $\lambda > 2\lambda_{min}$. When $2 < M < 3$ this gap in the Q mosaic can be covered completely by the $U(2, 2, 1)$ inner RLPs of double rays, and when $3 < M < 4$ by adding the $U(3, 3, 1)$ inner RLPs of triple rays.

The second-order singles from $U(2, 1, 2)$ cover a substantial part of the $Q/2^3$ mosaic, and they can be supplemented by the $U(3, 2, 2)$ and $U(2, 2, 2)$ RLPs from double rays. As just implied the fractional coverage of singles is low when $M > 2$ in the region with $d^* < D^*/2$; similarly, the coverage of doubles is low when $M > 3$ in the region with $d^* < D^*/3$. We present in Table 4, for different M, statistics on the percentage coverage by singles, and by singles plus doubles. Values are given both for the $d^* \le D$ overall coverage of V_R (corresponding to the points in Fig. 7) and for coverage below $D^*/2$ and $D^*/3$.

At $M = 2$, the Q mosaic is entirely covered by $U(1, 1, 1)$ and the percentage of singles in the region with $d^* < D^*/2$ is high at 88·4% [the tail of $U(2, 1, 2)$ also contributes]. For larger M and $d^* < D^*/2$, the percentage of singles decreases fairly rapidly as M increases. At $M = 3$ the Q mosaic is covered by $U(1, 1, 1)$ and $U(2, 2, 1)$, and the percentage of singles plus doubles is high in the region with $d^* < D^*/3$, but it decreases for larger M.

Table 5 presents information about numbers in place of percentages. It will be recalled that the total number of RLPs in V_R is proportional to

$$D^{*4}(\lambda_{max} - \lambda_{min}) = D^{*4}(M - 1)\lambda_{min}.$$

For given D^*, the regions $d^* < D^*/2$ and $d^* < D^*/3$ contain only 1/16 and 1/81 of the total RLPs in V_R. To illustrate these aspects Table 5 shows the numbers of RLPs for different M assuming that a hemisphere of radius $D^* = 0{\cdot}5$ Å^{-1} ($d_{min} = 2{\cdot}0$ Å) contains 10 000 RLPs. The calculations assume that the $M = \infty$ case corresponds to $\lambda_{max} = 2{\cdot}5$ Å and $\lambda_{min} = 0$, and that the $M = 5, 3, 2$ cases correspond to $\lambda_{max} = 2{\cdot}5, 1{\cdot}5, 1{\cdot}0$ Å, respectively, with λ_{min} constant at 0·5 Å.

Though higher percentages are obtained with smaller values of M, the dominant feature of Table 5, as implied in § 7, is that the various totals for the full range $d^* \le D$ depend mainly on $(\lambda_{max} - \lambda_{min})$. The numbers of accessible RLPs in the region with $d^* < D^*/2$ are relatively small, but coverage there is much improved for large M when doubles as well as singles can be measured. Indeed, when M is large, measurement of triples would be helpful. Thus, when $M = 5$, the number of measurable RLPs for the full range of $d^* \le D^*$ would rise from 3567 in Table 5 to 3661, and in the $d^* < D^*/3$ range the number would rise from 19 to 35. In the limit of $M = \infty$, the total would rise from 4387 to 4531, and in the $d^* < D^*/3$ range the number would rise from 0 to 32.

9. The effect of a limited angular aperture

Previously we have assumed that all diffracted beams could intercept the detector (film). This is valid if

$$\theta_{acc} \ge \sin^{-1}(D^*\lambda_{max}/2) = \theta_{max}.$$

However, the angular acceptance will often be less than this, for example in an effort to reduce spatial overlap of spots (Greenhough & Helliwell, 1983; Helliwell, 1985). We shall refer to the effect as the θ-cut effect. The beams not intercepting the detector

obviously have a Bragg angle θ satisfying the inequality

$$\theta_{max} > \theta > \theta_{acc}.$$

In this section we ignore angular restrictions at low angle. In the X-ray case these may arise because of the direct-beam stop, but the size of the effect is very small.

Moreover, we assume that the detector is placed symmetrically with regard to the incident beam. Therefore, our analysis would not apply directly to the neutron time-of-flight method where the detector is placed off axis, nor would it apply to the X-ray case if the film is placed asymmetrically.

9.1. *The multiplicity distribution*

We know from § 8, Fig. 11(*e*), that the probability of a ray being single increases from 0·832 to 1·0 as $\theta \rightarrow \theta_{max}$ and $d^* \rightarrow D^*$ (from $D^*/2$). Hence, the rays excluded by a restricted detector aperture are predominantly single rays, which, along with doubles, are the ones that can be accurately measured.

Whereas the single rays are considerably affected as soon as $\theta_{acc} \leq \theta_{max}$, the same is not true of the double rays. The double rays contain RLPs in the regions $U(2,2,1)$, $U(2,2,2)$, $U(3,2,2)$, $U(3,2,3)$ *etc.* to $U(n,2,n)$, $U(n,2,n-1)$. As θ_{acc} is reduced the θ cut affects the nth regions first (Fig. 13) then the $(n-1)$th *etc.*, and finally the $U(2,2,1)$ and $U(2,2,2)$ regions. For the nth regions the θ cut-off begins to impinge at a $\theta_{n,2}$ of

$$\theta_{n,2} = \sin^{-1}[D^* \lambda_{max}(n-1)/2n].$$

The regions which contribute the most RLPs to the measured pattern, *via* double rays, are those with small n, *i.e.* $U(2,2,1)$, $U(2,2,2)$, $U(3,2,2)$ and $U(3,2,3)$. Hence, if

$$\theta_{acc} \geq \theta_{3,2} (> \theta_{2,2})$$

then the bulk of the double rays will be measured.

Similar considerations apply for the triple and higher m-tuple rays. The general version of the equation given earlier for doubles but now written for m-tuples is

$$\theta_{n,m} = \sin^{-1}[D^* \lambda_{max}(n-m+1)/2n].$$

The above statements regarding single, double and triple rays hold for $M \geq 3$. For $n \geq M$ or $M \leq 3$ the θ-cut effect is more complicated to visualize. However, for $M \leq 3$ the multiplicity distribution is then dominated by single rays; indeed for $1 < M < 2$ the rays involved are nearly all single. A θ-cut effect would not change the multiplicity distribution greatly in this case, although single rays would obviously be lost.

It should be noted that since any θ-cut line is a straight line from the origin the θ-cut effect never changes the multiplicity of a ray (other than to eliminate it completely).

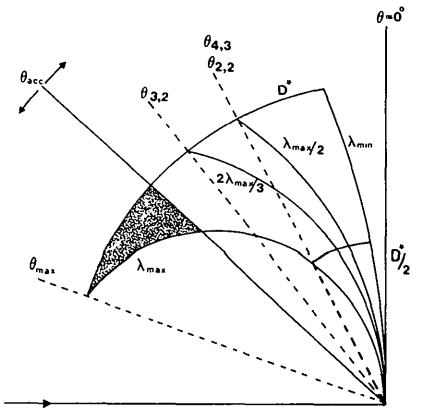

Fig. 13. The effect of a θ cut. Those stimulated beams which pass through the RLPs in the cross-hatched region do not intercept the detector. The diagram shows the positions of some key values of θ (*e.g.* θ_{max}; $\theta_{3,2}$; $\theta_{2,2} = \theta_{4,3}$) which delineate regions associated with the singles, doubles and triples. An arbitrary position of θ_{acc} is shown as well as $\theta = 0°$.

9.2. *Overall volume lost*

The overall volume V_R of stimulated reciprocal space is that lying between the D^*, λ_{max} and λ_{min} spheres, with $V_R = (\pi/4) D^{*4} (\lambda_{max} - \lambda_{min})$.

The θ-cut effect causes a volume V^- to be sliced off V_R (see Fig. 13). It can be shown that

$$V^- = (\pi/4) D^{*4} \lambda_{max} (1 - 4\mu/3 + \mu^4/3),$$

where $\mu = (\sin \theta_{acc} / \sin \theta_{max})$. The parameter μ will be used later to characterize the relative magnitude of the θ-cut effect in a given experimental situation (see § 9.3). The fraction of RLPs which are not measured is

$$V^- / V_R = [M/(M-1)](1 - 4\mu/3 + \mu^4/3).$$

For $\mu < 1$ the lost volume is at high d^*. The region of stimulated reciprocal space for $d^* < D^*/2$ is not affected by a θ cut until $\theta_{acc} < \theta_{2,2}$. Hence, the percentage coverage detailed in Table 4 below $D^*/2$ is not affected in most realistic experimental situations.

9.3. *Examples and results*

To illustrate the θ-cut effect we take one of the pea lectin Laue patterns detailed by Helliwell (1985). The value of the parameter μ for this pattern is 0·55. The experimental parameters were $D^* = (1/2{\cdot}6)$ Å^{-1}, $\lambda_{min} = 0{\cdot}45$ and $\lambda_{max} = 2{\cdot}6$ Å ($M = 5{\cdot}78$), film radius 59·3 mm and crystal-to-film distance 95 mm - see also the notes to Table 6.

Table 6 contains histograms, for different θ cuts ($0{\cdot}29 < \mu < 1{\cdot}0$), showing the number of recorded RLPs as a function of wavelength. The entry for $\mu = 0{\cdot}55$ corresponds exactly to Table 2(*a*) in

Helliwell (1985). The entry for $\mu = 1{\cdot}0$ shows, within statistical variations, a constant number of RLPs per unit wavelength interval as expected and a total which is the total number of stimulated RLPs. As μ decreases from 1·0 the longer wavelength bins show a decrease in the number of recorded RLPs. At $\mu =$ 0·55, 36% of the total RLPs are lost.

Table 7 shows the multiplicity distributions of the recorded Laue rays corresponding to the entries in Table 6. The entry for $\mu = 0{\cdot}55$ in Table 7 is slightly different from the equivalent entry in Table 2(*b*) of Helliwell (1985) owing to an improved method of computer simulation. The simulation for $\mu = 0{\cdot}69$ was chosen to illustrate the important point that as μ decreases from 1 a considerable reduction in the number of singles occurs before the rest of the distribution is affected. This is because $\theta_{acc} = 20{\cdot}1°$ is greater than $\theta_{3,2} = 19{\cdot}5$ or $\theta_{2,2} = 14{\cdot}5°$. For the triple rays $\theta_{4,3} = 14{\cdot}5$ and $\theta_{3,3} = 9{\cdot}6°$ and the region associated with $V(3, 3)$ is much larger than $V(4, 3)$. Hence it is not until the $\mu = 0{\cdot}29$ column in Table 7 that the number of triple rays is affected significantly. At $\mu =$ 0·29 only 2742 single rays are recorded out of the 12 630 stimulated.

It is clear from these results that the detector should be close enough and/or big enough to accept all θ values up to θ_{max} ($\mu = 1{\cdot}0$) to avoid loss of important single rays. However, a short crystal-to-detector distance leads to decreased spatial separation of spots and obviously the recorded pattern should not be so dense that spatial overlap of spots leads to the effective loss of many RLPs. A future paper will deal with the optimization of the detector arrangement taking account of the theory presented here but also dealing with the spatial-overlap effect.

10. Discussion and concluding remarks

10.1. *Comparison between theory, computer simulation and experiment*

The only direct experimental method in the X-ray case of determining the number of orders m that contribute to a Laue reflection is to examine each Laue reflection with an energy-sensitive detector. This is barely feasible for proteins. However, indirect methods exist which depend on the indexing of the Laue diffraction pattern; that is, identifying the ray h, k, l associated with each Laue reflection. The number of orders m contributing to each reflection may then be simply calculated for preliminary experimental estimates of D^*, λ_{max} and λ_{min}. These parameters, together with the unit-cell parameters and crystal orientation, may be further refined to yield more precise values of m for each reflection. The correctness of the indexing, and hence of the values of m, may be checked internally, for example by comparison of the intensities of symmetry-related rays, or of observed with calculated intensities (Wood *et al.*, 1983; Machin & Harding, 1985; Campbell, Habash, Helliwell & Moffat, 1986).

Histograms may be calculated which describe the number and proportion of Laue reflections, and of reciprocal-lattice points, that are single, double, triple and so on (Elder, 1984). Such histograms form the data against which we have tested our theory. Some are based on the indexing and refinement of Laue photographs obtained from protein crystals of known structure: pea lectin, phosphorylase b and hen egg white lysozyme; others are obtained from computer-simulated Laue patterns from crystals with primitive and non-primitive lattices, with a variety of space groups, cell dimensions, crystal orientations and maximum resolutions, and with several wavelength ranges and detector acceptance angles.

Since each experimental Laue photograph yields only a limited number of parameters (for example, the proportion of reflections that are single, double, triple, quadruple and greater than quadruple), a full test of our theory has required extensive reliance on computer-simulated data. We emphasize that the simulations in no way depend on or utilize the multiplicity of Laue reflections; rather, multiplicities are derived results. Secondly, in all cases so far examined, the simulations accurately reproduce experimental data, in both the location of the Laue reflections and their structure amplitudes.

The agreement between our theory and the experimental or computer-simulated results is shown in Figs. 7 and 9, where the curves are obtained from theory and the points are experimental or computer simulated. Agreement is very satisfactory. The scatter of points about the lines may be accounted for by the fact that the theory deals with volumes, which are then related to numbers of points *via* the reciprocal-cell volume V^* (§ 2). Fluctuations in the number of points will occur that depend on the exact crystal orientation, and will be proportionately larger, the smaller the number of points. Deviations between our theory and experiment appear to be of this quasi-random nature, rather than systematic.

As noted in § 2, our theory is based on primitive lattices. At first sight, it might appear that the theory would require modification to apply to face-centred or body-centred lattices, where the relations between h, k and l may lead to the systematic absence of, say, all odd-order reflections. Such is not the case; one theory encompasses both primitive and non-primitive lattices. We note that indexing on a non-primitive lattice is a convention for mathematical convenience, which has no physical interaction with or effect on the diffraction pattern; all lattices can be indexed as primitive. Indeed, computer simulation of Laue diffraction patterns from a cubic lattice of constant cell dimension led to the same proportion of multiple reflections if the lattice were primitive, face-centred

Table 6. *Distribution of recorded RLPs in each wavelength interval as a function of* θ_{acc}

	θ_{acc} (°)	30	20·1	16·0	12·7	8·2
Maximum λ in each bin (Å)	Crystal-to-film distance (mm)	34	70	95	125	200
	μ	1·0	0·69	0·55	0·44	0·29
0·593		1018	1018	1018	1018	1018
0·737		970	970	970	970	970
0·880		977	977	977	977	729 ←
1·023		996	996	996	996	386
1·167		973	973	973	970 ←	213
1·310		1001	1001	1001	731	137
1·453		1011	1011	1008 ←	480	87
1·597		964	964	747	309	51
1·740		1008	1008	546	223	42
1·883		975	928 ←	388	152	25
2·027		982	685	284	112	28
2·170		991	548	233	107	20
2·313		963	370	145	56	9
2·457		993	330	137	44	9
2·600		984	245	95	42	10
Total		14 806	12 024	9518	7187	3734
Number *lost* due to θ cut		0	2782	5288	7619	11 072
Percentage *lost* due to θ cut (%)		0	19	36	52	75

Notes

1. The symbol ← shows the first bin in each histogram affected by the θ cut.
2. The specific case treated is that for pea lectin (Helliwell, 1985). The third column ($\mu = 0{\cdot}55$) was presented previously in Helliwell (1985).
3. Experimental conditions for PERQ prediction:

   $\lambda_{min} = 0{\cdot}45$, $\lambda_{max} = 2{\cdot}6$ Å; $\varphi = 30°$, $\delta\varphi_x = 0{\cdot}1239$, $\delta\varphi_y = 0{\cdot}1282$, $\delta\varphi_z = -0{\cdot}6254°$; $d_{min} = 2{\cdot}6$ Å; reciprocal cell: $a^* = 0{\cdot}0200322$, $b^* = 0{\cdot}0166559$, $c^* = 0{\cdot}007447$ Å^{-1}. Film radius = 59·3 mm.
4. Each wavelength bin is 0·144 Å wide.

Table 7. *The multiplicity distributions of recorded Laue rays as a function of* θ_{acc}

		Number recorded				
	θ_{acc} (°)	30	20·1	16·0	12·7	8·2
Multiplicity of Laue ray	Crystal to film distance (mm)	34	70	95	125	200
	μ	1·0	0·69	0·55	0·44	0·29
1		12 630	9863 ←	7524	5431	2742
2		704	695	649 ←	559	282
3		121	122	109	101	64 ←
4		43	43	41	35	25
5		21	21	18	16	12
6		3	3	2	2	1
7		7	7	6	6	5
8		3	3	3	3	1
9		1	1	1	1	1
10		1	1	1	1	0
18		1	1	1	1	1
Total number of RLPs		14 806	12 024	9518	7187	3734
Total number of Laue rays		13 535	10 760	8355	6156	3134

Notes

1. The symbol ← indicates when a sizeable cut on the singles, doubles, triples has occurred.
2. Experimental conditions are as for Table 6.

or body-centred (though the absolute number of these reflections of course differed).

The theory also predicts that the proportions of multiple reflections are independent of the limiting crystal resolution D^* (provided $D^*_{max} < 2/\lambda_{max}$). That is, it will apply equally to crystals of small molecules or of simple inorganic compounds with cell dimensions of a few ångströms, and to crystals of macromolecules such as viruses with cell dimensions of hundreds of ångströms which diffract to different D^*. Here, too, agreement between theory and computer simulation is good. The only deviations occur for smaller unit cells, where the maximum indices are limited (§ 2) and there the fluctuations due to the smaller number of reflections are proportionally larger.

10.2. *Main findings*

Perhaps the most striking conclusion is that, even for the widest wavelength range that is readily accessible (say $0{\cdot}3 < \lambda < 3{\cdot}0$ Å), the proportion of reciprocal-lattice points that lie on single rays exceeds 83%. The remaining 17% are non-randomly distributed in reciprocal space (§ 8).

A second important conclusion is that the total number of single (and double) reflections is to a good approximation directly proportional to the wavelength range: the wider is the range, the more quantifiable data are accessible. Thus, a major advantage of the Laue method, namely the simultaneous stimulation of numerous Bragg reflections, is not accompanied by a more severe multiple-orders problem. The advocacy by Helliwell (1984, p. 1468, 1985) of a somewhat wider wavelength range than that originally used by Moffat and colleagues (Moffat *et al.*, 1984; Bilderback *et al.*, 1984) is therefore justified. However, there are other experimental circumstances in which a more restricted wavelength range is advantageous (Moffat, Szebenyi & Bilderback, 1984).

Thirdly, the effects of restricted angular acceptance of the detector are severe (§ 9). Data are lost when diffracted beams from stimulated reflections are not intercepted by the detector. The large majority of the lost reflections are single, and thus are potentially quantifiable data. We emphasize that in the Laue case a restriction on θ is not simply a restriction on resolution, as it is in the monochromatic case. The lost reflections are predominantly, but not entirely, at high resolution and are largely stimulated by the longer wavelengths. The effects of a restriction on θ_{max} may be seen in Table 6, where the number of reflections per wavelength interval is initially constant, then falls off with increasing wavelength as the restriction comes into play. The same problem affects the data obtained on phosphorylase b (Hajdu *et al.*, 1986). Of course, the restriction on θ_{acc} is determined by the need to minimize the loss of RLPs suffering spatial overlap. This is discussed further later.

Although the multiple-orders problem is evidently not as serious as was initially believed, there are two further complexities associated with the Laue method which must be solved if it is to become a major structure-solving technique. Extraction of precise structure amplitudes from measured intensities requires, among other steps, the derivation and application of wavelength-dependent correction factors. A variety of strategies to determine these factors and accomplish the processing of Laue data is under development (Helliwell, 1985; Clifton *et al.*, 1985; Campbell *et al.*, 1986; Smith, Szebenyi, Schildkamp & Moffat, unpublished results). These are derived from the highly successful strategies for quantification of oscillation photographs (Arndt & Wonacott, 1979; Rossmann, 1979; Rossmann, Leslie, Abdel-Meguid & Tsukihara, 1979).

The second complexity is that quantification of a Laue diffraction pattern requires that adjacent Laue reflections be clearly distinguished from each other. The very large number of reflections in a typical Laue pattern, obtained with wide wavelength range from a crystal with a densely populated reciprocal lattice, means that the average angular separation between each reflection and its nearest neighbour is small. For certain crystal orientations, reflections in principal zones may have angular separations that are substantially less than average. These constitute what Helliwell (1985) denotes 'spatial overlaps', as distinct from the exact overlaps of multiple orders, 'energy overlaps'. The proportion of Laue reflections designated as spatial overlaps in principle depends on the crystal-to-detector distance, the diffracted beam size, the method of peak-profile fitting employed, the unit-cell parameters, the crystal orientation and the wavelength range. It may be substantial, as in the initial example provided by Helliwell (1985).

The theory we have presented has considerable implications for the future collection of Laue data, in such areas as the nature of the X-ray source (bending magnet, wiggler or undulator); choice of X-ray optics (reflection and transmission X-ray mirrors, multilayers and filters); design of the Laue camera to minimize unwanted angular restrictions, yet maintain the ability to separate adjacent reflections; and choice of detector (film, image plate or electronic). Data-collection strategies can be devised to cover that small proportion of reflections found as multiple orders at a single crystal setting, and to exploit the symmetry of the diffraction pattern, for crystals belonging to systems other than triclinic. These experimental topics will be considered at length in a subsequent paper (Helliwell & Moffat, in preparation).

The University of York, the Science and Engineering Research Council (SERC) and SERC Daresbury Laboratory are especially thanked for support. KM

is grateful to the Royal Society and the John Simon Guggenheim Foundation for financial support during his sabbatical leave in Daresbury and York; his research at Cornell is supported by NIH grant RR-01646. The authors are especially grateful to M. Elder, P. A. Machin and staff at the SERC, Daresbury Laboratory for the provision and development of the software used in the computer simulations. DWJC thanks Dr M. M. Harding of the University of Liverpool for stimulating early discussions on the Laue method.

Note added during publication. It is with great sadness that we have to record that M. Elder and P. A. Machin of Daresbury Laboratory died in a climbing accident on 7 March 1987.

References

AMORÓS, J. L., BUERGER, M. J. & AMORÓS, M. C. (1975). *The Laue Method.* New York: Academic Press.

ARNDT, U. W. & WONACOTT, A. J. (1979). *The Rotation Method in Crystallography.* Amsterdam: North-Holland.

BILDERBACK, D. H., MOFFAT, K. & SZEBENYI, D. M. E. (1984). *Nucl. Instrum. Methods*, **222**, 245-251.

CAMPBELL, J., HABASH, J., HELLIWELL, J. R. & MOFFAT, K. (1986). *CCP4 Newsletter*, No. 18. Daresbury Laboratory, Warrington, England.

CHRISTOPHER, J. (1956). *Am. Math. Mon.* **63**, 399-401.

CLIFTON, I. J., CRUICKSHANK, D. W. J., DIAKUN, G., ELDER, M., HABASH, J., HELLIWELL, J. R., LIDDINGTON, R. C., MACHIN, P. A. & PAPIZ, M. Z. (1985). *J. Appl. Cryst.* **18**, 296-300.

ELDER, M. (1984). Fortran program *LGEN* for PERQ computer. Unpublished work.

GREENHOUGH, T. J. & HELLIWELL, J. R. (1983). *Prog. Biophys. Mol. Biol.* **41**, 67-123.

HAILS, J., HARDING, M. M., HELLIWELL, J. R., LIDDINGTON, R. & PAPIZ, M. Z. (1984). Daresbury Laboratory preprint DL/SCI 479E, Warrington, England.

HAJDU, J., MACHIN, P., CAMPBELL, J. W., CLIFTON, I. J., ZUREK, S., GOVER, S. & JOHNSON, L. N. (1986). *CCP4 Newsletter*, No. 17. Daresbury Laboratory, Warrington, England.

HARDY, G. H. & WRIGHT, E. M. (1979). *An Introduction to the Theory of Numbers*, 5th ed. Oxford: Clarendon Press.

HEDMAN, B., HODGSON, K. O., HELLIWELL, J. R., LIDDINGTON, R. & PAPIZ, M. Z. (1985). *Proc. Natl. Acad. Sci. USA*, **82**, 7604-7607.

HELLIWELL, J. R. (1984). *Rep. Prog. Phys.* **47**, 1403-1497.

HELLIWELL, J. R. (1985). *J. Mol. Struct.* **130**, 63-91.

MACHIN, P. A. & HARDING, M. M. (1985). Editors. *CCP4 Newsletter*, No. 15. Daresbury Laboratory, Warrington, England.

MOFFAT, K., SCHILDKAMP, W., BILDERBACK, D. H. & VOLZ, K. (1986). *Nucl. Instrum. Methods*, A**246**, 617-623.

MOFFAT, K., SZEBENYI, D. & BILDERBACK, D. (1984). *Science*, **223**, 1423-1425.

RABINOVICH, D. & LOURIE, B. (1987). *Acta Cryst.* A. In the press.

ROSSMANN, M. G. (1979). *J. Appl. Cryst.* **12**, 225-238.

ROSSMANN, M. G., LESLIE, A. G. W., ABEL-MEGUID, S. S. & TSUKIHARA, T. (1979). *J. Appl. Cryst.* **12**, 570-581.

RUMSEY, H. (1966). *Duke Math. J.* **33**, 263-274.

SCHULTZ, A. J., SRINIVASAN, K., TELLER, R. G., WILLIAMS, J. M. & LUKEHART, C. M. (1984). *J. Am. Chem. Soc.* **106**, 999-1003.

WOOD, I. G., THOMPSON, P. & MATTHEWMAN, J. C. (1983). *Acta Cryst.* B**39**, 543-547.

ZUREK, S., PAPIZ, M. Z., MACHIN, P. A. & HELLIWELL, J. R. (1985). *CCP4 Newsletter*, No. 16. Daresbury Laboratory, Warrington, England.

Acta Cryst. (1987). A**43**, 674-676

A Modified Asymptotic Development of the Density Distribution of a Structure Factor in $P\bar{1}$

BY J. BROSIUS

Département de Mathématiques, Université du Burundi, BP2700, Burundi

(*Received* 9 *January* 1987; *accepted* 2 *April* 1987)

Abstract

A concise and very precise formula has been obtained for the density of a structure factor in space group $P\bar{1}$ under the assumption that the atomic position vectors are distributed uniformly and independently over the unit cell.

1. Introduction

Let $E_{\mathbf{h}} = (2/N^{1/2}) \sum_{j=1}^{N/2} \cos(2\pi \mathbf{r}_j . \mathbf{h})$ denote the normalized structure factor for reciprocal-lattice vector $\mathbf{h}$ in space group $P\bar{1}$ for a unit cell containing N equal atoms. Now let $\mathbf{x}_1, \mathbf{x}_2, \ldots, \mathbf{x}_n$ ($n = N/2$) be n random vectors that are distributed independently and uniformly over the unit cell and consider the random variable

$$\hat{E}_{\mathbf{h}} = (2/N^{1/2}) \sum_{j=1}^{n} \cos(2\pi \mathbf{x}_j . \mathbf{h}) \qquad (n = N/2). \quad (1)$$

Let us denote by $E \to p(E)$ the probability density of the random variable $\hat{E}_{\mathbf{h}}$.

0108-7673/87/050674-03$01.50